ADVANCED MATERIALS
www.advmat.de

Observation of Topological Edge States in Thermal Diffusion

Hao Hu, Song Han, Yihao Yang, Dongjue Liu, Haoran Xue, Gui-Geng Liu, Zheyu Cheng, Qi Jie Wang, Shuang Zhang, Baile Zhang,* and Yu Luo**

Topological band theory predicts that bulk materials with nontrivial topological phases support topological edge states. This phenomenon is universal for various wave systems and is widely observed for electromagnetic and acoustic waves. Here, the notion of band topology is extended from wave to diffusion dynamics. Unlike wave systems that are usually Hermitian, diffusion systems are anti-Hermitian with purely imaginary eigenvalues corresponding to decay rates. By direct probe of the temperature diffusion, the Hamiltonian of a thermal lattice is experimentally retrieved, and the emergence of topological edge decays is observed within the gap of bulk decays. The results of this work show that such edge states exhibit robust decay rates, which are topologically protected against disorder. This work constitutes a thermal analogue of topological insulators and paves the way to exploring defect-immune heat dissipation.

1. Introduction

The topology of crystal's band structures has gained increasing attention in condensed matter physics since the 1980s.[1–4] The topological band theory has revolutionized our understanding on classifications of matter and, as a consequence, many fundamentally new topological electronic materials have been discovered, including topological insulators[5–8] and topological semimetals.[9] In parallel, the analogy between the quantum mechanical and classical waves has inspired the generalization of numerous concepts in condensed matter physics to the classical-wave systems such as electromagnetic, acoustic, and mechanical wave systems. Intuitively, one can transform the governing equations of classical waves (e.g., Maxwell equations for electromagnetic waves) into the Hamiltonian formulation. Following this methodology, topological phases initially proposed for quantum-mechanical waves have been recently realized in various classical-wave systems,[10–17] enabling many practical applications such as topological lasers,[18–21] robust optical delay lines,[22] and high quality on-chip communication.[23,24] Recent advances have further extended the topological states from Hermitian to non-Hermitian wave systems,

H. Hu, S. Han, D. Liu, Q. J. Wang, Y. Luo
School of Electrical and Electronic Engineering
Nanyang Technological University
50 Nanyang Avenue, Singapore 639798, Singapore
E-mail: luoyu@ntu.edu.sg

Y. Yang
Interdisciplinary Center for Quantum Information
State Key Laboratory of Modern Optical Instrumentation
ZJU-Hangzhou Global Scientific and Technological Innovation Center
Zhejiang University
Hangzhou 310027, China
E-mail: yangyihao@zju.edu.cn

Y. Yang
International Joint Innovation Center
Key Lab. of Advanced Micro/Nano Electronic Devices
and Smart Systems of Zhejiang
The Electromagnetics Academy at Zhejiang University
Zhejiang University
Haining 314400, China

The ORCID identification number(s) for the author(s) of this article can be found under https://doi.org/10.1002/adma.202202257.

DOI: 10.1002/adma.202202257

Y. Yang
Jinhua Institute of Zhejiang University
Zhejiang University
Jinhua 321099, China

H. Xue, G.-G. Liu, Z. Cheng, Q. J. Wang, B. Zhang
Division of Physics and Applied Physics
School of Physical and Mathematical Sciences
Nanyang Technological University
21 Nanyang Link, Singapore 637371, Singapore
E-mail: blzhang@ntu.edu.sg

Q. J. Wang, B. Zhang
Centre for Disruptive Photonic Technologies
Nanyang Technological University
21 Nanyang Link, Singapore 637371, Singapore

S. Zhang
Department of Physics
University of Hong Kong
Hong Kong 999077, China

S. Zhang
Department of Electrical and Electronic Engineering
University of Hong Kong
Hong Kong 999077, China

particularly parity-time symmetric wave systems,[25] enabling many intriguing phenomena such as parity-time symmetric topological edge states,[26] topological funneling,[27] bulk Fermi arcs,[28] and many others.[29–32]

Another important natural existing physical dynamics, known as diffusion, has been widely studied in the context of heat transfer,[33] Brownian motion,[34] and so on. Unlike fields in wave systems (quantum mechanical or classical), diffusive fields are not governed by "frequency", and thus the phase no longer depends on time but solely on space. These fundamental differences between wave and diffusive fields prevent the direct extension of the band theory and topological concepts from wave to diffusion systems. A recent theoretical attempt has shown that the concept of topological phases can be applied to the heat diffusion, which is manifested as topologically robust interfacial thermal decay rates within the gap of bulk decay rates.[35] Yet, such topological states of diffusion have not been experimentally observed.

Here, we transfer the notion of topological phases to diffusion dynamics and explore the topological heat diffusion experimentally. Fundamentally different from the usually Hermitian topological states in wave systems,[36–38] the topological states in diffusion systems are intrinsically anti-Hermitian, and thus the corresponding eigenvalue ω is purely imaginary. Such an imaginary eigenvalue corresponds to a decay rate γ as $\gamma = \mathrm{Im}(\omega)$.[39] In other words, for diffusive dynamics, the topological band theory applies to the decay rates rather than to the frequencies as in wave systems. As a physical consequence, the topological thermal state decays exponentially in time with a protected rate, while the topological wave state oscillates periodically in time at a protected frequency.[40] Moreover, as the phase of fields in the topological diffusion system is time-invariant, this remarkable property enables us to readily retrieve the Hamiltonian via direct measurement of the temperature distribution in time. We highlight that the experimental retrieval of the Hamiltonian is fundamentally important in the investigation of topological physics but has never been directly accomplished so far.

2. Results and Discussion

For the practical implementation of our topological diffusion system, we construct a 1D thermal lattice consisting of periodic aluminum disks (aluminum alloy 6061-T6) with radius $r = 1$ cm connected via aluminum channels, with height $h = 1$ cm and lattice constant $a = 7$ cm (see the design and photograph of the sample in **Figure 1**a,b). The straight and meandering channels are judiciously designed in our experiment to control the effective thermal diffusivity (denoted as D_1 or D_2) between two disks. The structured channels have geometric parameters $d = 2$ mm, $w = 1$ mm, and $g = 1.3$ mm.

The demonstrated topological thermal lattice is an excellent thermal analogue of the Su–Schrieffer–Heeger (SSH) model that initially describes electrons hopping on an atomic chain (see the upper panel of Figure 1a). The disk in the thermal lattice corresponds to the atom in the original SSH model while staggered effective diffusivities D_1 and D_2 between disks mimic staggered hopping amplitudes t_1 and t_2 between atoms. Very recently, a theoretical study[35] showed that, in a lattice structure

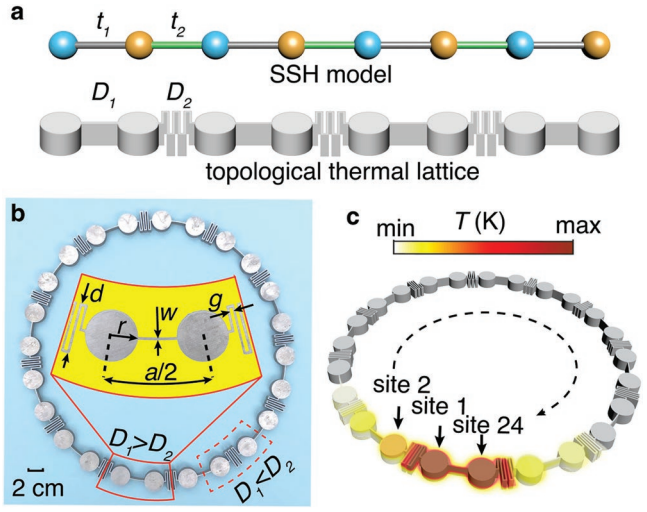

Figure 1. Design of a topological thermal lattice with periodic boundary condition. a) Comparison between the SSH model and the topological thermal lattice. The effective diffusivity of the thermal field between two disks is determined by the structured channel. The staggered effective diffusivities D_1 and D_2 of the thermal field in the thermal lattice correspond to the staggered hopping amplitudes t_1 and t_2 in the SSH model. b) Photograph of the topological thermal lattice consisting of 12 unit cells and 24 sites. Two types of unit cells are highlighted: the one enclosed by the solid curve, and the other enclosed by the dashed curve. c) Schematics of the temperature distribution in the thermal lattice when site 1 of the structure is heated. The sites are numbered clockwise.

similar to our design, the governing discretized thermal diffusion equation takes the form as (see derivation details in Section S1, Supporting Information),

$$\partial \overline{T}(t) / \partial t = -\mathrm{i} H \overline{T}(t) \tag{1}$$

where the solution $\overline{T}(t) = [T_1(t) \quad T_2(t) \quad \cdots \quad T_{j_x}(t) \quad \cdots]^T$ of the discretized thermal diffusion equation is the temperature field as a function of spatial and temporal coordinates. The element of the temperature field $\overline{T}(t)$ corresponds to the on-site temperature $T_{j_x}(t)$ (with j_x corresponding to the site index), which is solely dependent on time only if the site is sufficiently small and highly conductive. As each thermal disk only couples to the two nearest neighbouring ones, the corresponding Hamiltonian H of the system is tridiagonal. As a result, the designed thermal topological lattice with N disks depicted in Figure 1b has an $N \times N$ Hamiltonian given by

$$H = (-\mathrm{i}) \begin{bmatrix} D_1 + D_2 & -D_1 & 0 & 0 & \cdots & -D_2 \\ -D_1 & D_1 + D_2 & -D_2 & 0 & \cdots & 0 \\ 0 & -D_2 & D_1 + D_2 & -D_1 & \cdots & 0 \\ 0 & 0 & -D_1 & D_1 + D_2 & \cdots & 0 \\ \vdots & \vdots & \vdots & \vdots & \ddots & \vdots \\ -D_2 & 0 & 0 & 0 & \cdots & D_1 + D_2 \end{bmatrix} \tag{2}$$

where D_1 and D_2 denote the effective intradiffusivity and interdiffusivity, respectively, normalized to $(a/2)^2$ (see derivation details in Sections S1 and S2, Supporting Information). Note that the values of D_1 and D_2 depend on the geometry of the unit cell, for example, $D_1 > D_2$ corresponds to the unit cell

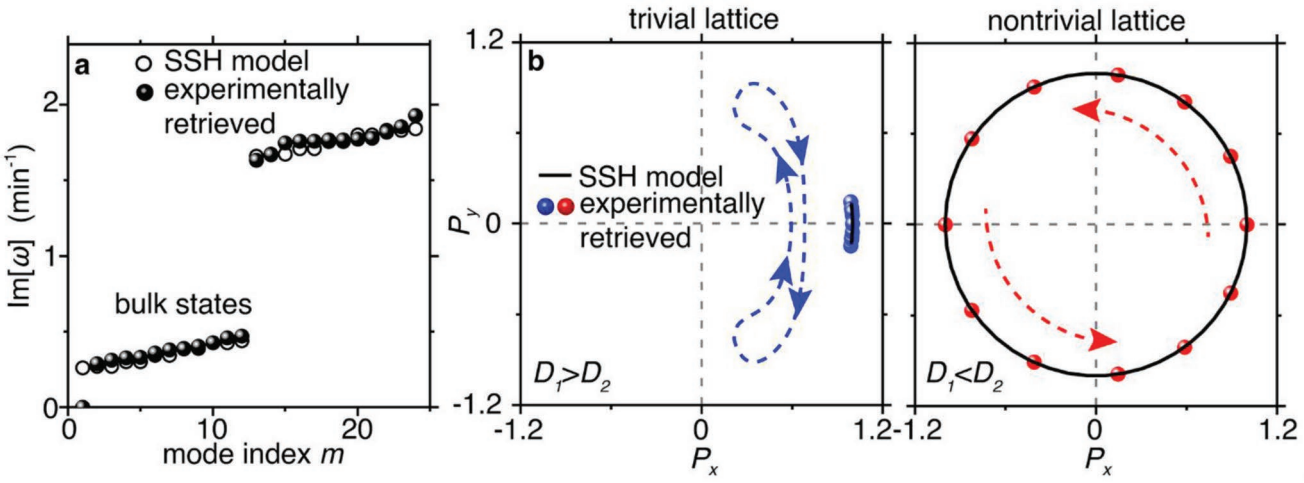

Figure 2. Experimentally retrieved decay rates of eigenmodes and topological invariants. a) Spectrum of decay rates retrieved from measured Hamiltonian. b) The paths of the endpoints of the pseudospin vector $\overline{P} = P_x\hat{x} + P_y\hat{y}$ on the P_xOP_y plane (i.e., the equatorial plane of the Bloch sphere) for the lower band of decay rates. The winding number equals the loop number of the endpoints of pseudospin vector that encircles the origin, when k_x goes through the Brillouin zone from 0 to 2π. The evolution trajectory of endpoints of the pseudospin vector is indicated by dashed arrows. In the left part of (b), the studied unit cell has $D_1 > D_2$, while in the right part, the studied unit cell has $D_1 < D_2$.

with a straight intracell channel and a meandering intercell channel (as indicated by the region enclosed by the solid curve in Figure 1b), while $D_1 < D_2$ corresponds to the unit cell with meandering intracell channel and straight intercell channel (as indicated by the region enclosed by the dashed curve in Figure 1b). In this way, the diffusion equation is related to the well-known SSH model initially proposed for the quantum systems. As both D_1 and D_2 are real numbers in our case, H is an anti-Hermitian version of Hamiltonian in the original SSH model, and its eigen values ω are purely imaginary.

We first measure the bulk states in the topological thermal lattice with the periodic boundary condition. As shown in Figure 1b,c, the fabricated sample has 12 unit cells in total. An igniter is used to locally heat up an individual site numbered as j_x of the designed structure. To obtain a set of on-site temperatures on the structure, a thermal camera (FLIR T620) is employed to record the transient heat transfer in the sample at different moments. We implement 24 groups of measurement by heating up each site in sequence to construct the temperature matrix $\hat{\mathrm{T}}(t) = [\,\overline{T}_1 \quad \overline{T}_2 \quad \cdots \quad \overline{T}_{24}\,]$, where $\overline{T}_i$ is the temperature field composed of 24 on-site temperatures. The transient heat transfer process follows $\overline{T}(t) = e^{-\mathrm{i}Ht}\overline{T}(0)$, and, therefore, the real-space Hamiltonian can be retrieved from the measured temperature matrix as

$$H_{\mathrm{exp}} = \mathrm{i}\frac{\ln[\hat{\mathrm{T}}(t_2)\hat{\mathrm{T}}^{-1}(t_1)]}{t_2 - t_1} \tag{3}$$

where $\hat{\mathrm{T}}(t_1)$ and $\hat{\mathrm{T}}(t_2)$ correspond to temperature matrices at different measurement moments t_1 and t_2, respectively. In the experiment, we choose t_1 = 0.1 min and t_2 = 0.4 min. Thanks to the time-invariant phase of diffusion fields, the retrieval procedure of the real-space Hamiltonian is greatly simplified in our case. In comparison, the measurement of the real-space Hamiltonian is fundamentally challenging in wave systems, whose phase varies rapidly over time. The measured 24×24 real-space Hamiltonian H_{exp} is provided in Supporting Information databases.

By solving the eigenvalues of the retrieved Hamiltonian H_{exp}, we obtain the spectrum of the thermal decay rates, and observe a complete decay-rate gap opened up between 1.67 and 1.85 min^{-1} (see the black dots in **Figure 2**a). Moreover, the retrieved Hamiltonian enables us to determine the topological invariants of the decay-rate bands (see calculation details in Section S5, Supporting Information). We have obtained the topological invariants of two types of unit cells in our experiments, that is, the one with $D_1 > D_2$, and the other with $D_1 < D_2$. As shown in Figure 2, although the spectra of decay rates for two unit cells are identical, the trajectories of the endpoints of the pseudospin vector $\overline{P} = P_x\hat{x} + P_y\hat{y}$ are different, that is, when $D_1 > D_2$ ($D_1 < D_2$), the trajectory does not (does) wind around the origin, corresponding to the topologically trivial (nontrivial) phase. Here, the pseudospin vector $\overline{P}$ is determined by Bloch functions retrieved from the measured Hamiltonian (see more explanations in Section S5, Supporting Information), and the winding number equals the loop number that its end point encircles the origin as the wavevector spans the entire Brillouin zone. As our lattice preserves sublattice symmetry, the winding number 0 (1) corresponds to a Zak phase of 0 (π). Our experimentally retrieved results are consistent with that using the SSH model, as shown in Figure 2.

Topological edge states arise at the domain wall between two topologically distinct thermal lattices. To illustrate this point, we experimentally probe the edge states at two types of domain walls, that is, domain wall *A* and domain wall *B*, as depicted in **Figure 3**a. In the domain wall *A* (*B*), the trivial and nontrivial domains are connected via a meandering (straight) channel, which mimics weak (strong) coupling (Figure 3b). From the measured real-space Hamiltonian, we observe two edge states (denoted as edge states I and II in the following discussion) emerging inside the decay-rate gap of bulk modes (see Figure 3c). Edge state I (II) shows a symmetric (asymmetric)

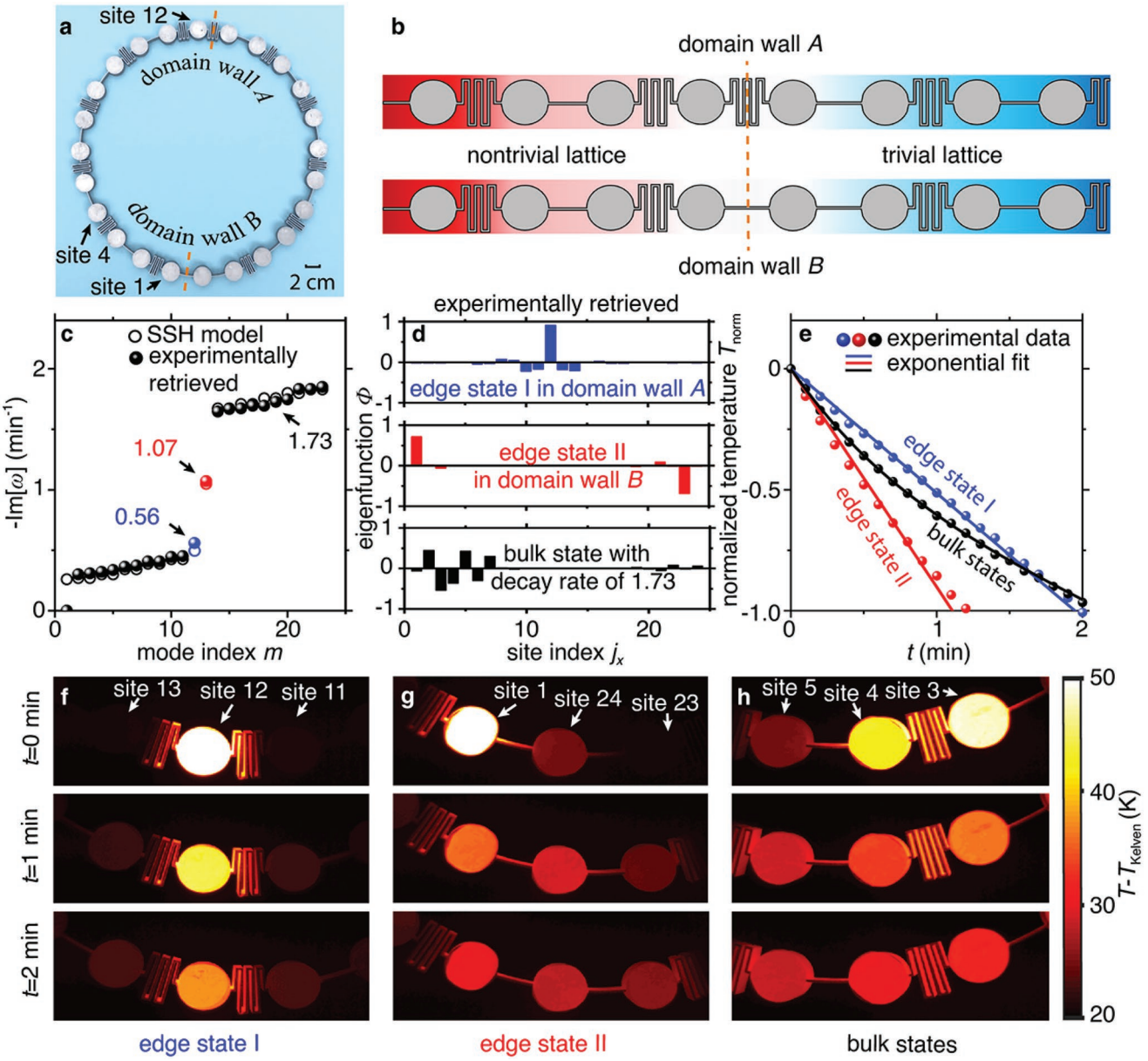

Figure 3. Observation of topological edge states. a) Photograph of the topological thermal lattice with domain walls. The dashed lines indicate the positions of domain walls. b) Schematics of domain wall *A* and *B*, respectively. c,d) Retrieved decay-rate bands and mode profiles in the topological thermal lattice. e) Time evolution of normalized temperature for edge states and bulk states. The temperature is normalized with $T_{norm} = \ln[(T - T_f)/(T_i - T_f)]$, where T_i is the temperature of heated site at $t = 0$ min and T_f is the room temperature. One exponential function with a decay rate of 0.52 (0.91) is sufficient to fit the measured time evolution of temperature for edge state I (edge state II), while two exponential functions with decay rates of 2.10 and 0.29 are required to well fit the time evolution of temperature for bulk states. f–h) Temperature field distribution for edge states and bulk states. The temperature field distributions are recorded at $t = 0$ min, $t = 1$ min, and $t = 2$ min, respectively.

mode profile at domain wall *A* (*B*), as depicted in Figure 3d. The difference between two edge states results from the different effective diffusivities of channels surrounding two domain walls. At domain wall *A*, site 12 and its neighboring sites are connected with the meandering channels of low effective diffusivity. Thus, most energy of edge state I is trapped on site 12. At domain wall *B*, site 24 and its neighboring sites are connected with the straight channels of high effective diffusivity. Thus, the energy of edge state II occupies site 24 and its neighboring sites, that is, site 1 and site 23. Owing to the emergence of these edge states, the domain-wall temperature decays at a different rate from that in the bulk. To verify this phenomenon experimentally, we excite edge and bulk states based on the mode distributions (Figure 3f–h), for example, edge state I (II) is excited by heating up site 12 (site 1) in the vicinity of the corresponding domain wall, while the bulk states are excited by heating up sites 3 and 4 in the bulk domain. Note that while the efficient excitation of the edge state II requires heating up site 1 and

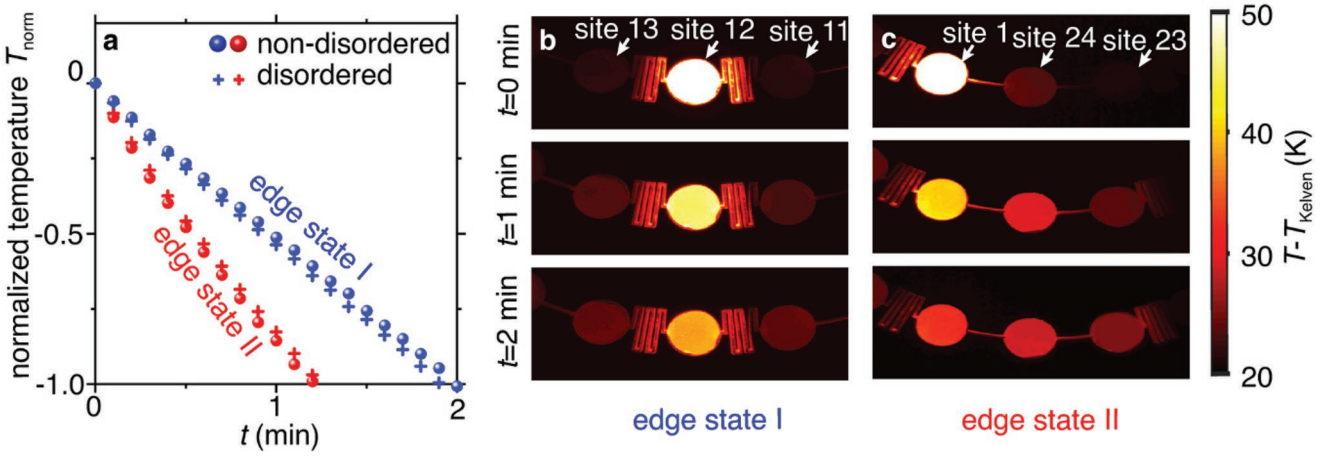

Figure 4. Influence of disorders on the topological edge states. a) Time evolution of normalized temperature for edge states in non-disordered and disordered systems, respectively. b,c) Temperature field distribution for edge states. The temperature field distributions are recorded at $t = 0$ min, $t = 1$ min, and $t = 2$ min, respectively.

cooling down site 23 simultaneously to match the temperature distribution of the eigenfunction, we only heat up site 1 in the experiment. Despite this experimental simplification, we find that solely heating up site 1 can sufficiently make the edge state II and thus, its diffusion behaviors dominate (see mode decomposition in Figure S10, Supporting Information). Then, the decay rate of each mode is determined by measuring the temperature of the heated site. Exponential functions are used to fit the temperature evolution to reveal different decaying processes of edge and bulk states (Figure 3e). Specifically, a single exponential function is sufficient to fit the temperature evolution of edge states (with the corresponding decay rate 0.52 min^{-1} for edge state I and 0.91 min^{-1} for edge state II). In other words, the edge states, once excited, decay at a constant rate in excellent agreement with the theoretical prediction in Figure 3c. Such a decay rate is insensitive to the environmental temperature, but is susceptible to the convection (Section S9, Supporting Information). In sharp contrast, two exponential functions are required to successfully fit the temperature evolution of bulk states at domain sites, with corresponding decay rates 2.10 and 0.29 min^{-1}, as the temperature decays rapidly at the beginning and more gently as time evolves. Such instability of the decay rate results from the excitation of multiple bulk modes in the bulk. Note that the excitation of a specific bulk state requires precisely assigning the initial on-site temperature according to the corresponding eigenfunction, while in our experiment, the implemented source profile shown in Figure 3h is a combination of multiple states (see mode decomposition in Figure S10, Supporting Information). The modes in the upper band of the decay rates are responsible for the fast decay in the early stage, while the modes in the lower band dominate in the slow decay after a while.

We also highlight that the two edge states are topologically protected and thus, robust against disorders. As our numerical calculations demonstrate that the effective diffusivity of the thermal channel is highly dependent on its height (see Figure S12, Supporting Information), we introduce a global disorder to the topological thermal lattice by randomly changing the height of each thermal channel. The measured results prove that the decay rate of edge states is robust against the disorders (see domain-wall temperature evolution and corresponding field distribution in **Figure 4**). This robustness is also corroborated by the experimentally retrieved spectrum of decay rates: the disorder dramatically changes the decay rates of the bulk states, for example, the decay-rate gap reduces from 0.18 to 0.10 in the presence of 30% disorders, whereas the topological edge states (i.e., states I and II) are immune to perturbations in diffusivity. The defect-immune decay rates and profiles make topological thermal edge states different from a general class of localized thermal modes without the topological protection (see more explanations in Section S10, Supporting Information).

3. Conclusion

In conclusion, our work provides the first experimental demonstration of the nontrivial topological phase and topological edge state in a diffusion system. Strikingly, our results hint that the notion of topological phases can apply to a general class of diffusion systems. Despite the time-invariant nature of our system studied here, the topological concept in principle can also be extended to time-dependent thermal diffusion systems.[39] Meanwhile, the powerful tool of topological analysis shown here could inspire future research in thermal functional materials with different types of topological phases in one, two, and three dimensions, including 2D and 3D topological insulators, Weyl semimetals, and high-order topological insulators.[41,42] The demonstrated topological states could find applications in temperature management and thermal information processing with topologically enabled robustness.[43]

4. Experimental Section

Experimental Method: The samples in the experiment were made of aluminum alloy 6061-T6 with the physical properties given by ref. [44]. The geometry was fabricated by wire electrical discharge machining with a fabrication tolerance of 0.1 mm. In the experiment, we used an igniter to heat up the designed sample locally (see the experimental setup in

Figure S5, Supporting Information). In each group of measurement, only one site was heated up. After a specific heating duration Δt, the FLIR T620 thermal camera was deployed to image the transient heat transfer in the thermal structure in time immediately. We had done 24 groups of measurement by heating up all the sites in the thermal structure accordingly to construct temperature matrix. The real-space Hamiltonian in the experiment was retrieved by extracting the temperature matrix $\hat{\mathrm{T}}(t)$ when $t_1 = 0.1$ min and $t_2 = 0.4$ min. The heating duration was $\Delta t = 0.3$ min.

Numerical Method: COMSOL Multiphysics was deployed to simulate the transient heat transfer process in the thermal structures. The numerical parameter setups for aluminum alloy 6061-T6 were: thermal conductivity $k = 180$ W m^{-1} K^{-1}, density $\rho = 2700$ kg m^{-3}, and heat capacity $C_\rho = 978$ J kg^{-1} K^{-1}. In the simulation, we also considered the convective heat flux of the environment with the heat transfer coefficient for convection being 18 W m^{-2} K^{-1}. Only one site in the thermal structure was heated up in each group of measurement. In each group of measurements, 24 on-site temperatures were obtained by recording the transient heat transfer of the thermal structure in time. 24 groups of measurements were conducted by heating up 24 sites in sequence, leading to 24 linearly independent temperature fields. The temperature matrix $\hat{\mathrm{T}}(t)$ was constructed by the 24 temperature fields. The real-space Hamiltonian in simulation was retrieved by extracting the temperature matrix $\hat{\mathrm{T}}(t)$ at $t_1 = 0.4$ min and $t_2 = 0.7$ min. The room temperature was set as 294.15 K. The initial temperature on the heated site was set as 333.15 K.

Supporting Information

Supporting Information is available from the Wiley Online Library or from the author.

Acknowledgements

H.H., S.H., and Y.Y. contributed equally to this work. This work was sponsored by the Singapore Ministry of Education (No. MOE2018-T2-2-189 (S), MOE2019-T2-2-085, and MOE2016-T3-1-006), A*STAR AME IRG Grant (No. A20E5c0095) and Programmatic Funds (No. A18A7b0058), the National Research Foundation Singapore Competitive Research Program (No. NRF-CRP18-2017-02, NRF-CRP22-2019-0006, and NRF-CRP23-2019-0007), the Research Grants Council of Hong Kong (No. AoE/P-701/20), and the National Natural Science Foundation of China (NNSFC) (No. 62175215).

Conflict of Interest

The authors declare no conflict of interest.

Data Availability Statement

The data that support the findings of this study are available from the corresponding author upon reasonable request.

Keywords

thermal diffusion, thermal functional materials, topological insulators

Received: March 10, 2022
Revised: June 1, 2022
Published online:

[1] F. D. M. Haldane, *Phys. Rev. Lett.* **1988**, *61*, 2015.
[2] D. C. Tsui, H. L. Stormer, A. C. Gossard, *Phys. Rev. Lett.* **1982**, *48*, 1559.
[3] D. J. Thouless, M. Kohmoto, M. P. Nightingale, M. den Nijs, *Phys. Rev. Lett.* **1982**, *49*, 405.
[4] S. Nakajima, T. Tomita, S. Taie, T. Ichinose, H. Ozawa, L. Wang, M. Troyer, Y. Takahashi, *Nat. Phys.* **2016**, *12*, 296.
[5] M. Z. Hasan, C. L. Kane, *Rev. Mod. Phys.* **2010**, *82*, 3045.
[6] X.-L. Qi, S.-C. Zhang, *Rev. Mod. Phys.* **2011**, *83*, 1057.
[7] C-Z. Chang, J. Zhang, X. Feng, J. Shen, Z. Zhang, M. Guo, K. Li, Y. Ou, P. Wei, L.-L. Wang, Z.-Q. Ji, Y. Feng, S. Ji, X. Chen, J. Jia, X. Dai, Z. Fang, S.-C. Zhang, K. He, Y. Wang, L. Lu, X.-C. Ma, Q.-K. Xue, *Science* **2013**, *340*, 167.
[8] K. He, Y. Wang, Q. K. Xue, *Natl. Sci. Rev.* **2014**, *1*, 38.
[9] A. Burkov, *Nat. Mater.* **2016**, *15*, 1145.
[10] T. Kariyado, Y. Hatsugai, *Sci. Rep.* **2016**, *5*, 18107.
[11] T. Yoshida, Y. Hatsugai, *Phys. Rev. B: Condens. Matter Mater. Phys.* **2019**, *100*, 054109.
[12] Z. Wang, Y. Chong, J. D. Joannopoulos, M. Soljačić, *Nature* **2009**, *461*, 772.
[13] L. Lu, J. D. Joannopoulos, M. Soljačić, *Nat. Photonics* **2014**, *8*, 821.
[14] A. B. Khanikaev, G. Shvets, *Nat. Photonics* **2017**, *11*, 763.
[15] Z. Yang, F. Gao, X. Shi, X. Lin, Z. Gao, Y. Chong, B. Zhang, *Phys. Rev. Lett.* **2015**, *114*, 114301.
[16] S. D. Huber, *Nat. Phys.* **2016**, *12*, 621.
[17] G. Ma, M. Xiao, C. T. Chan, *Nat. Rev. Phys.* **2019**, *1*, 281.
[18] B. Bahari, A. Ndao, F. Vallini, A. El Amili, Y. Fainman, B. Kanté, *Science* **2017**, *358*, 636.
[19] M. A. Bandres, S. Wittek, G. Harari, M. Parto, J. Ren, M. Segev, D. N. Christodoulides, M. Khajavikhan, *Science* **2018**, *359*, 1231.
[20] G. Harari, M. A. Bandres, Y. Lumer, M. C. Rechtsman, Y. D. Chong, M. Khajavikhan, D. N. Christodoulides, M. Segev, *Science* **2018**, *359*, 1230.
[21] Y. Zeng, U. Chattopadhyay, B. Zhu, B. Qiang, J. Li, Y. Jin, L. Li, A. G. Davies, E. H. Linfield, B. Zhang, Y. Chong, Q. J. Wang, *Nature* **2020**, *578*, 246.
[22] M. Hafezi, E. A. Demler, M. D. Lukin, J. M. Taylor, *Nat. Phys.* **2011**, *7*, 907.
[23] Y. Yang, Y. Yamagami, X. Yu, P. Pitchappa, J. Webber, B. Zhang, M. Fujita, T. Nagatsuma, R. Singh, *Nat. Photonics* **2020**, *14*, 446.
[24] Q. Yang, D. Wang, S. Kruk, M. Liu, I. Kravchenko, Y. Kivshar, I. Shadrivov, *arXiv: 2201.10750*, **2022**.
[25] S. K. Gupta, Y. Zou, X. Y. Zhu, M. H. Lu, L. J. Zhang, X. P. Liu, Y. F. Chen, *Adv. Mater.* **2020**, *32*, 1903639.
[26] L. Xiao, X. Zhan, Z. H. Bian, K. K. Wang, X. Zhang, X. P. Wang, J. Li, K. Mochizuki, D. Dim, N. Kawakami, W. Yi, H. Obuse, B. C. Sanders, P. Xue, *Nat. Phys.* **2017**, *13*, 1117.
[27] S. Weidemann, M. Kremer, T. Helbig, T. Hofmann, A. Stegmaier, M. Greiter, R. Thomale, A. Szameit, *Science* **2020**, *368*, 311.
[28] H. Zhou, C. Peng, Y. Yoon, C. W. Hsu, K. A. Nelson, L. Fu, J. D. Joannopoulos, M. Soljačić, B. Zhen, *Science* **2018**, *359*, 1009.
[29] F. Mostafavi, C. Yuce, O. S. Maganã-Loaiza, H. Schomerus, H. Ramezani, *Phys. Rev. Res.* **2020**, *2*, 032057.
[30] S. Longhi, *Phys. Rev. Lett.* **2020**, *124*, 066602.
[31] W. Tang, X. Jiang, K. Ding, Y.-X. Xiao, Z.-Q. Zhang, C. T. Chan, G. Ma, *Science* **2020**, *370*, 1077.
[32] K. Kawabata, K. Shiozaki, M. Ueda, M. Sato, *Phys. Rev. X* **2019**, *9*, 041015.
[33] L. D. Landau, E. M. Lifshitz, *Statistical Physics*, 3rd ed., Course of Theoretical Physics, Vol. *5*, Elsevier, Amsterdam, The Netherlands **1980**.
[34] A. Einstein, *Investigations on the Theory of the Brownian Movement*, Courier Corporation, New York **1956**.

[35] T. Yoshida, Y. Hatsugai, *Sci. Rep.* **2021**, *11*, 888.
[36] A. Blanco-Redondo, I. Andonegui, M. J. Collins, G. Harari, Y. Lumer, M. C. Rechtsman, B. J. Eggleton, M. Segev, *Phys. Rev. Lett.* **2016**, *116*, 163901.
[37] Y. Wang, Y.-H. Lu, F. Mei, J. Gao, Z.-M. Li, H. Tang, S.-L. Zhu, S. Jia, X.-M. Jin, *Phys. Rev. Lett.* **2019**, *122*, 193903.
[38] M. Xiao, Z. Zhang, C. T. Chan, *Phys. Rev. X* **2014**, *4*, 021017.
[39] Y. Li, Y.-G. Peng, L. Han, M.-A. Miri, W. Li, M. Xiao, X.-F. Zhu, J. Zhao, A. Alù, S. Fan, C. W. Qiu, *Science* **2019**, *364*, 170.
[40] P. St-Jean, V. Goblot, E. Galopin, A. Lemaître, T. Ozawa, L. L.e Gratiet, I. Sagnes, J. Bloch, A. Amo, *Nat. Photonics* **2017**, *11*, 651.
[41] B. Xie, H.-X. Wang, X. Zhang, P. Zhan, J.-H. Jiang, M. Lu, Y. Chen, *Nat. Rev. Phys.* **2021**, *3*, 520.
[42] M. Hu, Y. Zhang, X. Jiang, T. Qiao, Q. Wang, S. Zhu, M. Xiao, H. Liu, *Light Sci. Appl.* **2021**, *10*, 1.
[43] G. Xu, Y. Yang, X. Zhou, H. Chen, A. Alù, C.-W. Qiu, *Nat. Phys.* **2022**, *18*, 450.
[44] Y. J. Chao, X. Qi, *J. Mater. Process. Manuf. Sci.* **1998**, *7*, 215.